Delamination Damage Identification in Composite Shell Structures based on Inverse Finite Element Method and Refined Zigzag Theory

A. Kefal

Faculty of Engineering and Natural Sciences, Sabanci University, Istanbul, Turkey

Integrated Manufacturing Technologies Research & Application Center, Sabanci University, Istanbul, Turkey

Composite Technologies Center of Excellence, Sabanci University-Kordsa, Istanbul, Turkey

A. Tessler

Structural Mechanics and Concepts Branch, NASA Langley Research Center, Virginia, USA

ABSTRACT: The inverse finite element method (iFEM) is a viable and well-known shape-sensing method developed for continuous real-time monitoring of engineering structures by using only strain gauge measurements collected from discrete positions of the structure. In this paper, a novel damage-detection strategy for composite and sandwich shell structures is developed using a computational algorithm based on the iFEM coupled with a state-of-the-art single-layer theory, refined zigzag theory (RZT). The new strategy uses only strain gauge measurements taken from the on-board sensors to predict the size and location of delamination damage. Initially, the in-plane location and delamination size are identified. Subsequently, through-the-thickness locations are identified by examining the influence of the zigzag kinematics on the strain response of the laminated structure. The fundamental advantage of this computational approach is that it does not require any a priori knowledge of loading conditions, and it is also applicable to a general class of laminated composite and sandwich structures. The applicability of the new damage detection strategy is examined for various structural models with a delaminated region, and the damage prediction accuracy of iFEM-RZT is proved through comprehensive comparative study of results.

1 INTRODUCTION

Composite materials and sandwich structures have been widely used as primary load bearing structures in marine vessels, civil and military aircrafts, launch vehicles, and wind turbine blades, to name a few. Over the service life of a structure, however, the load carrying capability, strength, and structural integrity are likely to diminish due to such failure modes as delamination and fiber/matrix cracking (Tabrizi et al., 2019). Cyclic accumulation of such failures at different positions of the structure may lead to a catastrophic failure of the structure, thereby directly affecting environmental and human safety and resulting in direct economic losses. To avoid from these undesirable events, composite structures often require a viable application of structural health monitoring (SHM).

In general, SHM is an integrated technology to allow real-time collection of accurate structural integrity information to be used for condition-based maintenance scheduling. To enable effective SHM, robust and efficient shape and stress sensing algorithms capable of performing real-time, full-field structural integrity assessment are required (Gherlone et al., 2018). An important step of SHM is the structural damage detection which can enable the identification of damage location, size, and amount of material degradation.

Originally developed by Tessler & Spangler (2005), the inverse finite element method (iFEM), is a general and robust algorithm for performing real-time shape-sensing analysis, i.e., reconstruction of structural displacements from the information provided by a network of in-situ strain sensors. The shape-sensing information is also the fundamental constituent for reconstructing such structural response quantities as strain, stress, and failure. For these reasons, over the last decade the iFEM methodology has attracted considerable attention in the field of SHM (Kefal & Oterkus, 2015, Papa et al., 2017, Liu et al., 2018).

Prior to the introduction of iFEM, various other inverse methods were proposed to solve shape sensing of beam bending (Davis et al., 1996, Kim & Cho, 2004) and real-time monitoring of plate bending problems (Jones et al., 1998). All these methods, however, lack at least one of the main attributes inherent in iFEM algorithm. Primarily, these attractive shape-sensing capabilities are (i) no requirement of any loading and/or material information, (ii) applicability to complex structural geometry and/or boundary conditions, (iii) rapid process capability suitable for real time, and (iv) stable and accurate solutions even when a few sensor measurements are

available. Therefore, the iFEM methodology fulfills most crucial prerequisites of an on-board SHM system.

Numerous theoretical, computational, and experimental research studies have been conducted using the iFEM methodology. Some of the pioneering examples for plates and shell structures include the development of a three-node triangular inverse-shell element, iMIN3 (Tessler & Spangler, 2004), a four-node quadrilateral inverse-shell element, iQS4 (Kefal et al., 2016), an efficient curved inverse-shell element, iCS8 (Kefal, 2020), and isogeometric iFEM formulation (Kefal & Oterkus, 2020). Recently, Abdollahzadeh et al. (2020), presented a review and comparison study of several C^0-continuous iFEM elements, including various benchmark test cases for validation of new iFEM elements.

Recent iFEM applications range from typical marine vehicles (Kefal & Oterkus, 2016) and offshore structures (Li et al., 2020) to aerospace structures (Miller et al., 2016, Esposito & Gherlone, 2020, Oboe et al., 2021). Moreover, sensor placement strategies (Roy et al., 2020), smoothing procedures (Kefal et al., 2021a), and pre-extrapolation/curve-fitting approaches (Oboe et al., 2021) have been proposed to improve shape-sensing capabilities of iFEM by utilizing a lower number of sensors. In addition, various experimental test setups have been proposed for validation of the iFEM formulations (Colombo, et al., 2021, Kefal et al., 2021b). Also, several computational and laboratory experiments have been carried out using iFEM for structural damage identification (Colombo et al., 2019, Li et al., 2020, Roy et al., 2021).

For shape- and stress-sensing of laminated composite and sandwich shell structures, more advanced iFEM formulations have been proposed by Cerracchio et al. (2015) and Kefal et al. (2017). These new formulations employed the Refined Zigzag Theory, RZT (Tessler et al. 2010), which is used as a kinematic basis for iFEM. The latest formulation (Kefal et al., 2017) that merges iFEM with RZT, herein referred to as iFEM-RZT, minimizes a weighted least-squares functional that uses the complete set of strain measures of RZT, that include the membrane, bending, transverse shear and zigzag section strains. The iFEM-RZT methodology enables an accurate representation of zigzag-like deformations of highly heterogeneous and sandwich laminates to be represented across the laminate thickness.

In this effort, the iFEM-RZT approach is applied to detect delamination damage in laminated composite and sandwich shell structures for the first time in the literature. To this end, a new damage detection strategy is proposed by using principal section strain and curvature quantities reconstructed using suitable iFEM-RZT modeling. Several computational studies are presented to demonstrate the predictive capabilities of the present approach for identifying the location and size of delaminations using a relatively sparse set of strain sensors distributed on the structure.

2 iFEM-RZT FORMULATION

Consider a laminated composite plate being composed of N layers and located in a Cartesian global coordinate system $(x_1, x_2, z) \equiv (\mathbf{x}, z)$ as depicted in Figure 1. Adopting the single-layer theory representation, the displacement components of a material point within the laminate can be written in accordance with the kinematic relations of RZT (Tessler et al., 2010) as:

$$u_i^{(k)}(\mathbf{x}, z) = u_i + z\theta_i + \phi_i^{(k)} \psi_i \ (i = 1, 2) \tag{1a}$$

$$u_z(\mathbf{x}) = w \tag{1b}$$

$$\mathbf{u} \equiv [u_1 \quad u_2 \quad w \quad \theta_1 \quad \theta_2 \quad \psi_1 \quad \psi_2]^T \tag{1c}$$

where the (u_1, u_2, w), (θ_1, θ_2), and (ψ_1, ψ_2) represent the translational displacements, classical bending rotations, and zigzag rotations with the positive directions shown in Figure 1. Here, the $\mathbf{u} = \mathbf{u}(\mathbf{x})$ vector contains the seven kinematic variables of the RZT theory, i.e., the unknowns of a given boundary-value problem.
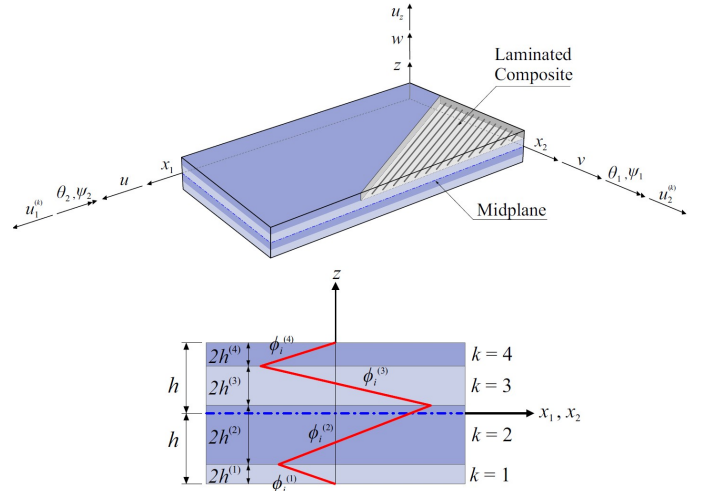

Figure 1. Directions of kinematic variables and through-the-thickness distribution of the zigzag functions.

The zigzag rotations are associated with piecewise linear zigzag functions to be able to account for highly zigzag in-plane displacement variations of thick sandwich structures. An example of the zigzag function's variation is present in Figure 1. Utilizing transverse-shear elastic moduli of the individual plies, these functions are originally established by Tessler et al. (2010) as:

$$\phi_i^{(k)} = z\beta_i^{(k)} + \alpha_i^{(k)} \quad (i = 1, 2) \tag{2a}$$

$$\beta_i^{(k)} = \frac{G_i}{Q_{ii}^{(k)}} - 1 \quad (i = 1, 2; \; k = 1, 2, ..., N) \tag{2b}$$

$$\alpha_i^{(k)} = \beta_i^{(k)} h + \sum_{j=2}^{k} 2h^{(j-1)} \left(\frac{G_i}{Q_{ii}^{(k)}} - \frac{G_i}{Q_{ii}^{(j-1)}} \right) (i = 1, 2) \tag{2c}$$

$$G_i = \left(\frac{1}{h} \sum_{j=1}^{N} \frac{h^{(j)}}{Q_{ii}^{(j)}} \right)^{-1} \quad (i = 1, 2) \tag{2d}$$

where the $\beta_i^{(k)}$ is the slope of the zigzag functions with respect to the thickness coordinate, $\alpha_i^{(k)}$ is the interlaminar-continuity coefficients of the zigzag functions, G_i is the average transverse-shear stiffness of the laminate, $2h^{(k)}$ and $2h$ terms stand for the full thickness of individual laminae, and laminate, respectively, $Q_{11}^{(k)}$ and $Q_{22}^{(k)}$ terms represent the transformed transverse-shear moduli of each ply for $x_1 z$- and $x_2 z$-planes, in the given order.

According to linear elasticity, the small strains can be defined by taking derivatives of Eq. (1a-b) as:

$$\boldsymbol{\varepsilon}^{(k)} = \mathbf{e}(\mathbf{u}) + z\boldsymbol{\kappa}(\mathbf{u}) + \boldsymbol{\mu}^{(k)}(\mathbf{u}, z) \tag{3a}$$

$$\boldsymbol{\gamma}^{(k)} = \mathbf{H}_\gamma^{(k)}(z)\boldsymbol{\gamma}(\mathbf{u}) + \mathbf{H}_\eta^{(k)}(z)\boldsymbol{\eta}(\mathbf{u}) \tag{3b}$$

where the vectors $\boldsymbol{\varepsilon}^{(k)}$ and $\boldsymbol{\gamma}^{(k)}$ define the in-plane and transverse-shear strains of k-th ply. In Eq. (3), the membrane, bending, and zigzag section strains of the laminate are given as:

$$\mathbf{e}(\mathbf{u}) = \begin{bmatrix} u_{1,1} & u_{2,2} & u_{1,2} + u_{2,1} \end{bmatrix}^T \tag{4a}$$

$$\boldsymbol{\kappa}(\mathbf{u}) = \begin{bmatrix} \theta_{1,1} & \theta_{2,2} & \theta_{1,2} + \theta_{2,1} \end{bmatrix}^T \tag{4b}$$

$$\boldsymbol{\mu}^{(k)}(\boldsymbol{u}) = \mathbf{H}_\phi^{(k)}(z) \begin{bmatrix} \psi_{1,1} & \psi_{2,2} & \psi_{1,2} & \psi_{2,1} \end{bmatrix}^T \tag{4c}$$

with

$$\mathbf{H}_\phi^{(k)} = \begin{bmatrix} \phi_1^{(k)} & 0 & 0 & 0 \\ 0 & \phi_2^{(k)} & 0 & 0 \\ 0 & 0 & \phi_1^{(k)} & \phi_2^{(k)} \end{bmatrix} \tag{4d}$$

Moreover, transverse-shear section strains of the laminate are derived as:

$$\boldsymbol{\gamma}(\mathbf{u}) \equiv \begin{bmatrix} \gamma_1 & \gamma_2 \end{bmatrix}^T = \begin{bmatrix} w_{,1} + \theta_1 & w_{,2} + \theta_2 \end{bmatrix}^T \tag{5a}$$

$$\boldsymbol{\eta}(\mathbf{u}) = \begin{bmatrix} \gamma_1 - \psi_1 & \gamma_2 - \psi_2 \end{bmatrix}^T \tag{5b}$$

which are associated with lamina-level constant matrices,

$$\mathbf{H}_\gamma^{(k)} = \begin{bmatrix} 1 + \beta_1^{(k)} & 0 \\ 0 & 1 + \beta_2^{(k)} \end{bmatrix} \tag{5c}$$

$$\mathbf{H}_\eta^{(k)} = \begin{bmatrix} -\beta_1^{(k)} & 0 \\ 0 & -\beta_2^{(k)} \end{bmatrix} \tag{5d}$$

in order to appropriately defined transverse-shear strains consistent with RZT. Note that the $\boldsymbol{H}_i^{(k)}$ $(i = \phi, \gamma, \eta)$ matrices are constant for any in-plane position, $\mathbf{x} = (x_1, x_2)$, and varies only as a function of z coordinate. On the other hand, the sections strains are dependent functions of the $\mathbf{x} = (x_1, x_2)$ coordinates while being constant through the thickness coordinate of the laminate, z.
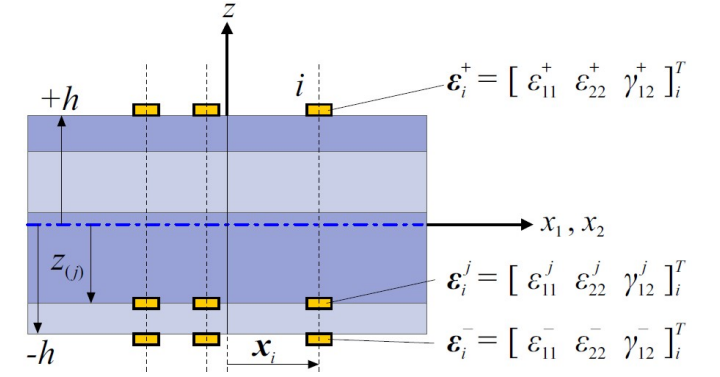

Figure 2. Experimental surface strain measurements.

The iFEM-RZT formulation uses experimentally measured section strain as the main input for performing deformation reconstruction of the laminate. Therefore, as depicted in Figure 2, the surface strain gauges should be patched on the top and bottom surfaces of the laminate, while fiber optic sensors should be embedded within the laminate between one of the interfaces of the two bonded laminae. The triaxial strain measurements obtained from a set of sensors at the position $\mathbf{x}_i = (x_1, x_2)_i$ $(i = 1, 2, ..., n)$, the experimental counterparts of the RZT section strains can be calculated as:

$$\mathbf{E}_i = \frac{1}{2}(\boldsymbol{\varepsilon}_i^+ + \boldsymbol{\varepsilon}_i^-) \quad (i = 1, 2, ..., n) \tag{6a}$$

$$\mathbf{K}_i = \frac{1}{2h}(\boldsymbol{\varepsilon}_i^+ - \boldsymbol{\varepsilon}_i^-) \quad (i = 1, 2, ..., n) \tag{6b}$$

$$\mathbf{M}_i^j = \boldsymbol{\varepsilon}_i^j - \mathbf{E}_i - z_{(j)}\mathbf{K}_i \quad (i = 1, 2, ..., n) \tag{6c}$$

where the symbols $\boldsymbol{\varepsilon}_i^+, \boldsymbol{\varepsilon}_i^-, \boldsymbol{\varepsilon}_i^j$ denote the experimental strains measured at top $z = +h$, and bottom $z = -h$, and j-th interface $z = z_{(j)}$ of the laminate. Note that these strain measurements are along the global axes, (x_1, x_2) at any i-th sensor position. Accordingly, at discrete positions of $\mathbf{x}_i$, the experimental membrane $\mathbf{E}_i$, bending $\mathbf{K}_i$, and zigzag $\mathbf{M}_i^j$ sections strains become available for an iFEM-RZT analysis in the real test environment.

Once these discrete strain measurements are gathered via strain rosettes as shown in Figure 2, they can be smoothed by using smoothing tech-

niques or fitted to continuous functions through surface/curve fitting techniques. To this end, smoothed iFEM formulation have recently been proposed by Kefal et al., which can be readily followed for obtaining continuous form of the experimental section strain. For mathematical convenience, we drop the '*i*' subscript from the experimental section strains by assuming that the smoothed section strains are enabled anywhere within the laminate domain. Experimental transverse-shear strains, $\mathbf{\Gamma}$ and $\mathbf{H}$, can be directly acquired from the surface strain sensor. However, following the smoothing procedure described in Kefal et al. (2021a), one can also calculate these experimental section strain in a continuous manner. Nevertheless, the contribution of the transverse-shear section strains to deformation reconstruction of a thin laminate is relatively much smaller than those of in-plane section strains. Thereby, the role of $\mathbf{\Gamma}$ and $\mathbf{H}$ can be safely omitted by setting these terms to zero during iFEM-RZT simulation.

The iFEM-RZT defines a weighted-least-squares functional to match the individual analytical strains with their experimental counterparts as:

$$\Phi(\mathbf{u}) = \frac{1}{V}\iiint_V \sum_i w_i \left\| \mathbf{\varphi}_i \right\|^2 dV \quad (i = e, \kappa, \mu, \gamma, \eta) \qquad (7a)$$

with the error functions of section strains defined as:

$$\mathbf{\varphi}_e \equiv \mathbf{e}(\mathbf{u}) - \mathbf{E} \qquad (7b)$$

$$\mathbf{\varphi}_\kappa \equiv \mathbf{\kappa}(\mathbf{u}) - \mathbf{K} \qquad (7c)$$

$$\mathbf{\varphi}_\mu \equiv \mathbf{\mu}^{(k)}(\mathbf{u}, z_{(j)}) - \mathbf{M}^j \qquad (7d)$$

$$\mathbf{\varphi}_\gamma \equiv \mathbf{\gamma}(\mathbf{u}) - \mathbf{\Gamma} \qquad (7e)$$

$$\mathbf{\varphi}_\eta \equiv \mathbf{\eta}(\mathbf{u}) - \mathbf{H} \qquad (7f)$$

In Eq. (7a), the symbol V denotes the volume of the laminate and the squared Euclidean norms of the $\mathbf{\varphi}_i$ vectors can be calculated as the dot product of vectors $\mathbf{\varphi}_i \cdot \mathbf{\varphi}_i$. Moreover, the w_i $(i = e, \kappa, \mu, \gamma, \eta)$ constants are positive weights that accounts for contributions of the individual section strains to the $\Phi(\mathbf{u})$ functional. In case any experimental is undetermined or not available in iFEM-RZT analysis, the associated weighting coefficient can be set to small number (e.g., 10^{-3}) as compared to unity, otherwise they will be one all the time. The least-squares functional can be discretized by utilizing suitable inverse-element implementations. For the numerical implementation of the new damage-detection strategy, a robust and computationally efficient three-node triangular inverse-shell element, i3-RZT (Kefal et al., 2017), is utilized. For this purpose, the kinematic variables are approximated related shape function, which can be directly used to define as induvial section strains as:

$$\chi(\mathbf{u}^e) = \mathbf{B}^\chi \mathbf{u}^e \quad (\chi = \varepsilon, \kappa, \mu, \gamma, \eta) \qquad (8)$$

where $\mathbf{u}^e$ represents the nodal degrees-of-freedom (DOF) vector of the i3-RZT element, and the $\mathbf{B}^\chi$ matrices establish the strain-displacement relations within the element domain through the derivatives of the shape functions. The explicit forms of these matrices can be found in Kefal et al. (2017).

Substituting Eq. (8) into Eq. (7a), and subsequently minimizing the resultant with respect to unknown displacement DOF, yields a set of element-level equations:

$$\frac{\partial \Phi(\mathbf{u}^e)}{\partial \mathbf{u}^e} = 0 \Rightarrow \mathbf{k}^e \mathbf{u}^e = \mathbf{f}^e \qquad (9)$$

where the left-hand-side matrix $\mathbf{k}^e$ is independent of the measured strain values (i.e., remain same during monitoring), and the right-hand-side vector $\mathbf{f}^e$ is a function of the measured strain values; these are updated for each strain-data acquisition. The element contributions to the global linear system of equations of the discretized structure are performed using the conventional finite element assembly procedures. Finally, the resulting system of equations can be solved by applying problem-specific kinematic boundary conditions, giving rise to the displacement solutions corresponding to the real-time strain measurements.

3 DAMAGE DETECTION STRATEGY

As the main goal for structural integrity assessment, iFEM-RZT can be used to identify the size and location of delamination damage. For this purpose, a novel damage-detection strategy is proposed herein by making quantitative assessment of principal section strains and curvatures calculated from iFEM-reconstructed displacements. The main benefit of this computational approach is that it does not require any loading information and uses only strain-gauge measurements taken from the on-board sensors to predict the size and location of delamination damage. Another advantage is that it can be successfully utilized in real-time monitoring applications. The approach is also applicable to a general class of laminated composite and sandwich structures.

Initially, the in-plane location and delamination size are identified. Once the displacement DOF are obtained, they can be utilized to obtain continuous section strains in each element domain. Then, the principal section strains can be evaluated at any point in the element domain as:

$$\varepsilon_{1,2}^\chi = \frac{\chi_1 + \chi_2}{2} \pm \sqrt{\left(\frac{\chi_1 - \chi_2}{2}\right)^2 + \left(\frac{\chi_3}{2}\right)^2} \quad (\chi = e, \kappa) \quad (10)$$

where e_1, e_2, e_3 and $\kappa_1, \kappa_2, \kappa_3$ are the vector components of membrane and bending section strains given in Eq. (4a-b), and $(\varepsilon_1^e, \varepsilon_2^e), (\varepsilon_1^\kappa, \varepsilon_2^\kappa)$ are the principle

section strains corresponding to the membrane and bending reactions of the laminate, respectively. Adopting the von Mises equations for plane stress, these principal section strains can be utilized to compute the equivalent section strains for the membrane and bending deformations as:

$$\varepsilon_{eq}^{\chi} = \sqrt{\left(\varepsilon_1^{\chi}\right)^2 - \varepsilon_1^{\chi}\varepsilon_2^{\chi} + \left(\varepsilon_2^{\chi}\right)^2} \quad (\chi = e, \kappa) \qquad (11)$$

The ε_{eq}^e and ε_{eq}^κ quantities are constant along the full thickness of the laminate and thus can be key indicators for identifying the in-plane position and shape of the delamination damage. Through-the-thickness locations of the delamination can be identified by examining the influence of the zigzag kinematics on the strain response of the laminated structure. For this purpose, average equivalent strain of each layer can be calculated as:

$$\overline{\varepsilon}_{eq}^{(k)} = \frac{1}{2h^{(k)}} \int_{z(k-1)}^{z(k)} \sqrt{(\varepsilon_1^{(k)})^2 - \varepsilon_1^{(k)}\varepsilon_2^{(k)} + (\varepsilon_2^{(k)})^2}\, dz \qquad (12)$$

where the symbols $(\varepsilon_1^{(k)}, \varepsilon_2^{(k)})$ represent the principal strains of individual layers, that are defined as:

$$\varepsilon_{1,2}^{(k)} = \frac{\varepsilon_{11}^{(k)} + \varepsilon_{22}^{(k)}}{2} \pm \sqrt{\left(\frac{\varepsilon_{11}^{(k)} + \varepsilon_{22}^{(k)}}{2}\right)^2 + \left(\frac{\gamma_{12}^{(k)}}{2}\right)^2} \qquad (13)$$

with $\varepsilon_{11}^{(k)}, \varepsilon_{22}^{(k)}, \gamma_{12}^{(k)}$ being components of in-plane strains $\boldsymbol{\varepsilon}^{(k)}$, i.e., linear/zigzag functions of the thickness coordinate as defined by Eq. (3a). Since the $\overline{\varepsilon}_{eq}^{(k)}$ strain is piecewise constant along the thickness of the laminate, this strain quantity may be a useful indicator for identifying the through-the-thickness position of the damage. Accordingly, percent difference between undamaged and damaged conditions of iFEM-RZT results can be compared to predict the damage evaluation in the laminate. For instance, the in-plane position of the damage can be predicted through the following damage detection parameters:

$$E_i^{\chi} = 100 \times \frac{\left|\left(\varepsilon_{eq}^{\chi}\right)_i^U - \left(\varepsilon_{eq}^{\chi}\right)_i^D\right|}{\left(\varepsilon_{eq}^{\chi}\right)_{max}^D} \quad (\chi = e, \kappa) \qquad (14)$$

where subscript $(i = 1, 2, ..., n_{el})$ denotes any position in an element domain, e.g., geometrical centroid of the element, with n_{el} being total number of inverse elements in an iFEM domain. In Eq. (14), the superscripts, U and D, are utilized to sort the equivalent strain quantities predicted using iFEM-RZT before and after damage instant, respectively. The maximum values of the Eq. (14) in the laminate domain can be utilized for identification of the in-plane damage position and its approximate shape. Besides, the thickness position of the damage can be examined through calculating the following percent difference for each layer available in the laminate as:

$$E_i^{(k)} = 100 \times \frac{\left|\left(\overline{\varepsilon}_{eq}^{(k)}\right)_i^U - \left(\overline{\varepsilon}_{eq}^{(k)}\right)_i^D\right|}{\left(\overline{\varepsilon}_{eq}^{(k)}\right)_{max}^D} \quad (i = 1, 2, ...n_{el}) \qquad (15)$$

The maximum values of the $E_i^{(k)}$ percent difference will shape the hot spot region in the layers, which can be exploited to indicate the actual delamination damage region and associated delaminated layers.

4 NUMERICAL RESULTS

Two different case studies are examined to validate the capabilities of the present computational strategy for delamination damage identification on the laminated composite plate and shell structures. Each problem has different types/positions of embedded delamination. To predict the damage locations in each problem, the detailed distributions of the displacements and strains reconstructed from sensor measurements by using iFEM are quantitatively examined in accordance with the formulas given in Section 3.

The first case study is a five-layer cross-ply cantilevered rectangular plate subject to torsion loading as depicted in Figure 3. The laminate is composed of symmetric lamina stacking sequence of 0/90/0/90/0 and each ply has the same thickness of 0.25 mm. All layers are made of carbon-epoxy material with the material properties listed in Table 1.

Table 1. Composite material properties (unit of moduli is GPa).

Material	Elastic Moduli	Poisson's Ratio	Shear Moduli
Carbon-Epoxy	$E_1^{(k)} = 157.9$	$\nu_{12}^{(k)} = 0.32$	$G_{12}^{(k)} = 5.93$
	$E_2^{(k)} = 9.584$	$\nu_{13}^{(k)} = 0.32$	$G_{13}^{(k)} = 5.93$
	$E_3^{(k)} = 9.584$	$\nu_{23}^{(k)} = 0.49$	$G_{23}^{(k)} = 3.227$
Glass-Epoxy	$E_1^{(k)} = 20.85$	$\nu_{12}^{(k)} = 0.341$	$G_{12}^{(k)} = 0.564$
	$E_2^{(k)} = 1.134$	$\nu_{13}^{(k)} = 0.341$	$G_{13}^{(k)} = 0.564$
	$E_3^{(k)} = 1.134$	$\nu_{23}^{(k)} = 0.356$	$G_{23}^{(k)} = 0.325$

The plate has the in-plane dimensions of 200×50 mm² and the span-to-thickness ratio is therefore 200/1.25 = 160, which is compatible with thin-plate classification. The left edge of the plate is fully clamped (no translation and no rotation) and the right edge is subjected to uniformly distributed torsional load, F_z = 80 N/m as shown in Figure 3.
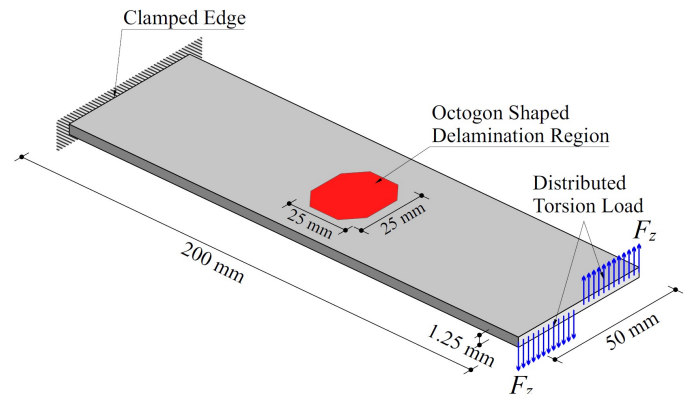

Figure 3. Laminated plate with a delaminated region.

In this case, the delamination damage is modelled by degrading material properties in octagon-shaped zone located at the center of the laminated plate. The actual layer of delamination damage is adjacent to the top bounding layer. Namely, the through-the-thickness position of damage is located under the top surface of the laminate, $k = 4$, considering that top and bottom layers are attributed to the $k = 1$ and $k = 5$, respectively. The "strain-sensor" (experimental strain) data and reference solutions are generated by performing high-fidelity direct FEM analyses. The "strain-sensor" data are used as input to the iFEM-RZT models, giving rise to the full-field displacement reconstruction. To this end, two different direct FEM analysis are performed: (1) plate without damage and (2) plate with damage in the fourth layer from the bottom surface of the laminate. Note that the damage is modelled through degrading elastic material constant of the undamaged material with the ratio of 10^{-3}.

Sensors are collected only along the perimeter of the plate as illustrated in Figure 4 on an iFEM-RZT domain. Thickness location of the sensors are top surface, bottom surface, and the interior location between first and second layers from the bottom surface of the plate. The weighting coefficients at elements having no sensors are set to 10^{-3} whereas they are adjusted to unity for elements having sensor data. Regarding the weighting coefficients of the transverse-shear measures, they are set to as 10^{-5} for all the elements.

- ■ Delaminated zone
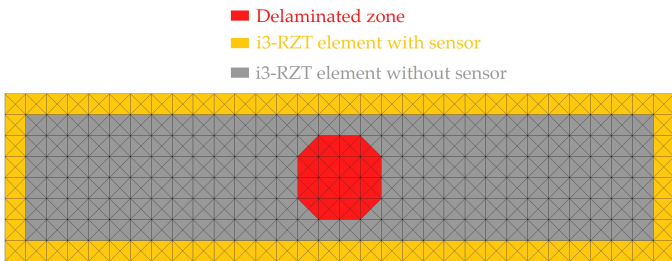- ■ i3-RZT element with sensor
- ■ i3-RZT element without sensor

Figure 4. iFEM-RZT discretization of the laminated plate composed of 1024 i3-RZT elements and 553 nodes.

Once the discrete strain-sensor data obtained for undamaged and damaged conditions are analyzed using same iFEM-RZT domain, the three-dimensional full-field displacements are accurately reconstructed. For brevity of the present section, these shape-sensing results are not included here. Subsequently, the reconstructed displacements are used to calculate strain and curvature data for each element in the discretization, as well as the principal strains, maximum shear strains, and equivalent strains corresponding to both damaged and undamaged laminates. Finally, these strain distributions are compared for the damaged and undamaged laminates to identify precise damage size and position.

The membrane and bending equivalent strains reconstructed using iFEM-RZT for undamaged and damaged conditions of the laminate are utilized to calculate the E^e and E^κ percent differences. As depicted in Figure 5, plotting these quantities over the laminate surface leads to the identification of in-plane delamination-damage position. In Figure 5, it is clearly observed that red contours of E^κ percent difference indicates the approximate shape of the hexagonal shape of the delaminated region. Moreover, the maximum values of the of E^e percent difference enables the localization of the damaged region as such drawing the top and bottom boundaries of the delamination zone.
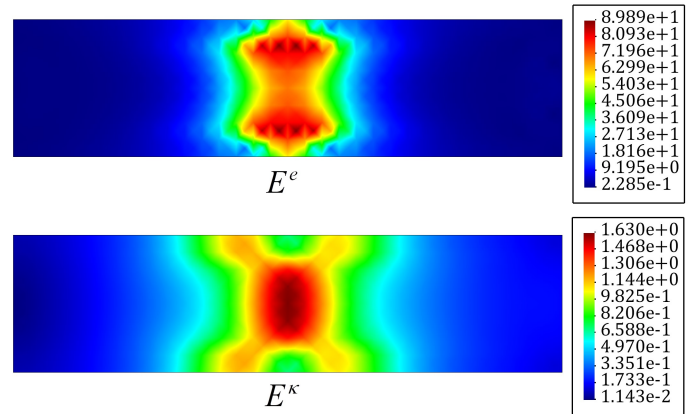

Figure 5. Contours of in-plane damage indicators, E^e and E^κ (Eq. 14), for laminated plate.
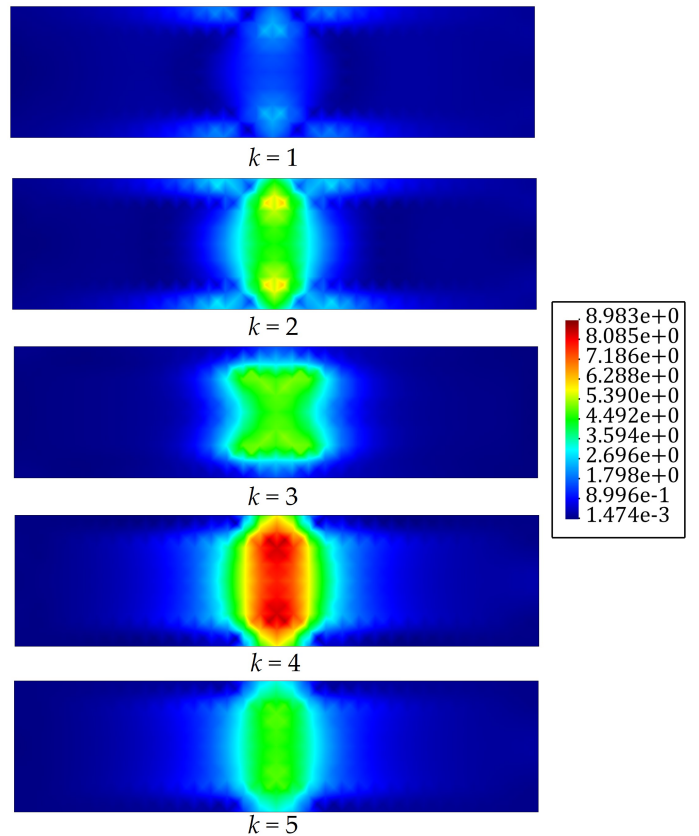

Figure 6. Contours of through-the-thickness damage indicator for laminate plate, $E^{(k)}$ (Eq. 15).

To account for the thickness position of the de-laminated layer, one can examine the lamina-level average equivalent strains and make comparison between undamaged and damaged instants of the laminate through Eq. (15). In this regard, the $E^{(k)}$ percent differences between pristine and degraded laminate conditions are plotted for each layer of the laminate in Figure 6. According to these contours, it can be clearly observed that red contours (maximum error) yield in the layer of $k = 4$, and this localized hot-spot region matches almost identically with exact location of the actual delaminated zone. Remarkably, according to the contours in Figure 6, it can be observed that the exact delamination zone affects its top and bottom layers under twisting loading condition, demonstrating superior deterministic accuracy of the iFEM-RZT analysis and proposed damage detection strategy.

The second case study is an eight-layer cross-ply shallow shell plate subject to distributed twisting loading as shown in Figure 7. Like the first test case, the laminae are stacked symmetrically with respect to the mid-surface of the shell, thereby constituting sequence of 0/90/0/90/90/0/90/0 with each ply having equal thickness of 0.55 mm. All layers are made of glass-epoxy material with the material properties listed in Table 1. Exact geometrical dimensions of the laminated shell as well as the applied constraint boundary conditions and force positions are clearly sketched in Figure 7. Here clamped edge is fully restraint against all translational and rotational kinematic variables, and the applied torsion has a magnitude of T_z = 10 N/m.
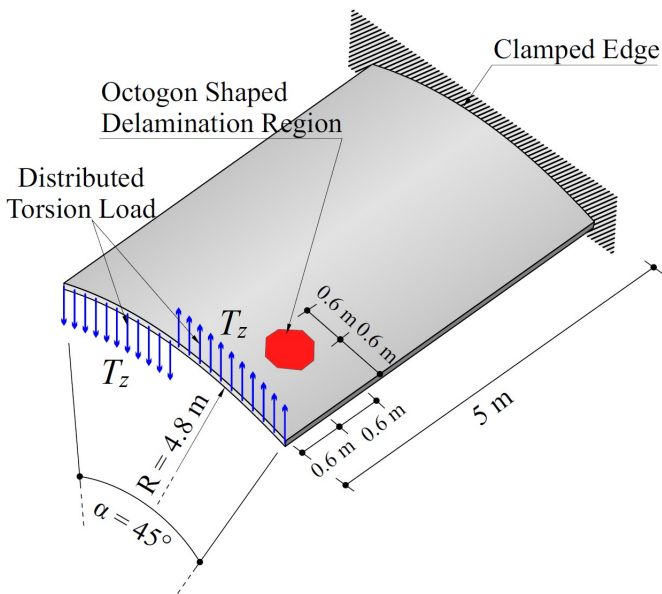

Figure 7. Laminated shallow shell with a delaminated region.

The delamination damage has an octagonal shape as proportionality depicted in Figure 7 and is located at the second layer from the bottom surface of the laminate, $k = 2$. Left edge is fully clamped and twisting load at the free edge. In fact, damage detec-tion on this geometry is very crucial as it can be considered as a representative of a floating large-scale marine composite panel. Therefore, the following iFEM-RZT analysis will reveal the practical merits of present damage detection approach for SHM of marine structures.

Firstly, a direct FEM analysis of the panel is performed to simulate the data collected from strain rosettes in case of undamaged and damaged conditions of the shell. For this purpose, the material properties of the pristine material at the second layer of the laminate within the shape of delaminated region are degraded with a ratio of 10^{-3}. Once the undamaged and damage discrete strain data obtained, they are directly used as an input for performing iFEM-RZT analysis. In this case, shape-sensing and damage detection analyses are conducted for two different sensor placement models, i.e., (1) full sensor pattern, and (2) sparse sensor pattern. In case of the full sensor patters, all the inverse shell element are provided with the sensor information, whereas the sparse model has only the sensors at the yellow elements depicted in Figure 8. Note that for both sensor placement model, the data is collected from top, bottom surfaces, and one of the interlaminar surfaces of the laminate. Since the thin-shell assumptions are suitable for the shallow, the weighting coefficients of the transverse-shear strains are adjusted to 10^{-5} for all iFEM-RZT analyses. Besides, the weighting coefficients associated with in-plane strains are set to 10^{-3} for the strain-less elements (an i3-RZT element without sensor) in the sparse sensor model.
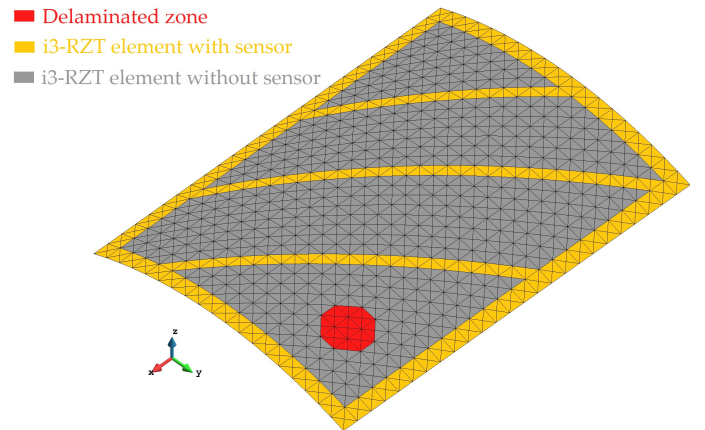

Figure 8. iFEM-RZT discretization of the shallow shell composed of 1900 i3-RZT elements and 995 nodes.

For each iFEM-RZT model, the reconstructed displacements are utilized to calculate equivalent strains, which subsequently become an input for damage detection procedure described in the previous section. In Figure 9, the percent difference of bending equivalent strains between undamaged and damaged scenarios of laminate are presented for both sensor placement models. As can be observed from the maximum values of E^κ damage indicator that the hot spot (red contours) regions are mainly

located in the delaminated region of the shallow shell (Figure 9). Expectedly, one-to-one mapping of strain measurements (full sensor pattern) provides better predictions than the sparse sensor pattern. However, considering the large amount of sensor data reduction in sparse model, overall trend of the E^κ variation over the in-plane geometry of the shell is captured very well, proving the damage detection capability of the sparse sensor placement model.
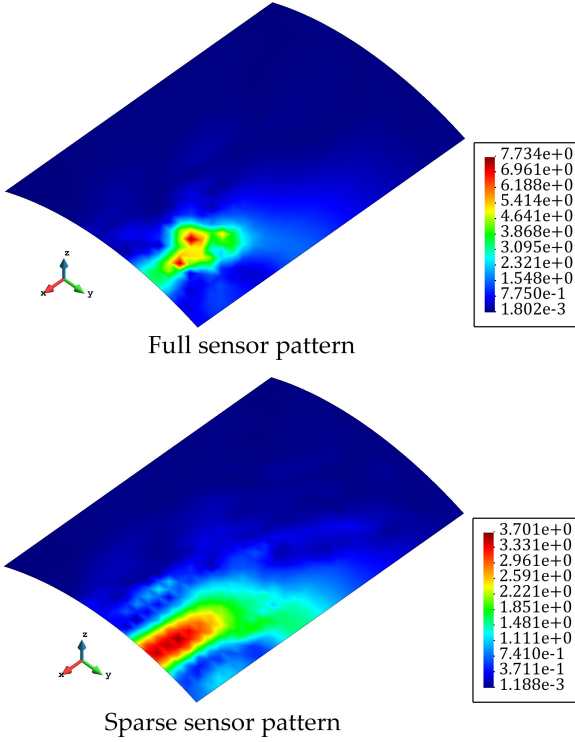

Full sensor pattern

Sparse sensor pattern

Figure 9. Comparison of in-plane damage indicator, E^κ (Eq. 14), contours predicted by full and sparse sensor patterns.
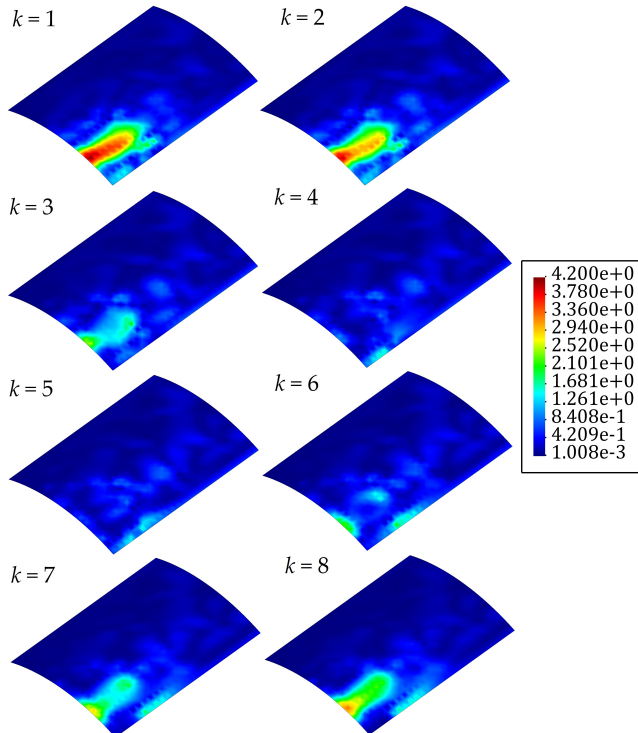

Figure 10. Contours of through-the-thickness damage indicator, $E^{(k)}$ (Eq. 15), predicted using sparse sensor pattern.

After the in-plane position and approximate shape of the damage region are identified, the through-the-thickness position of the delamination is also investigated by making comparison of the $E^{(k)}$ values calculated for each layer of the laminated shallow shell. To this end, we only investigate the sparse sensor pattern results to demonstrate the practical applicability of the approach to a real-life application, since the number of sensors is immensely reduced in the sparse sensor configuration. According to the results presented in Figure 10, the maximum values of the damage indicator are mainly localized in the first and second layers of the shell. This iFEM-RZT result apparently identifies the approximate position of the damage as being located either within the first or second layer of the laminate, which is quite close to the actual position of the delamination. Considering that the laminate is composed of a relatively large number of layers, it can be concluded that these indicators provide adequate identification of the delamination thickness zones. Hence, the superior accuracy of the present iFEM-RZT approach is rigorously confirmed for delamination damage identification of both laminated plate and shell structures, even with sparse sensor deployments.

5 CONCLUSIONS

A novel damage detection formulation is presented for composite structures by leveraging the shape-sensing information reconstructed from sensor measurements using an efficient iFEM-RZT formulation. The iFEM-RZT mathematical formulation is established by minimizing a weighted least-squares functional that uses the complete set of section strains of RZT, that include the membrane, bending, transverse shear and zigzag section strains. The recently introduced three-node inverse-shell element (i3-RZT) is implemented and used throughout the computational studies.

In these studies, strain solutions obtained from high-fidelity direct finite element models are used to represent the "experimentally measured" strain data. To enable damage identification, principal section strain and curvature quantities are reconstructed for each element in the iFEM-RZT discretization, leading to the computation of the appropriate delamination failure criteria and damage indexes. Initially, the in-plane location and delamination size are identified. Subsequently, through-the-thickness locations are identified by examining the influence of the zigzag kinematics on the strain response of the laminated structure. It is demonstrated that the iFEM-RZT methodology can provide high-quality identification of delamination damage, with the potential for application to more complex composite structures.

6 ACKNOWLEDGEMENT

7 REFERENCES

Abdollahzadeh, M.A., Kefal, A., & Yildiz, M., 2020. A comparative and review study on shape and stress sensing of flat/curved shell geometries using C0-continuous family of iFEM elements. *Sensors*, 20(14), p. 3808.

Cerracchio, P., Gherlone, M., Di Sciuva, M., & Tessler, A. 2015. A novel approach for displacement and stress monitoring of sandwich structures based on the inverse finite element method. *Composite Structures, 127*, 69-76.

Colombo, L., Sbarufatti, C. & Giglio, M. 2019. Definition of a load adaptive baseline by inverse finite element method for structural damage identification. *Mechanical Systems and Signal Processing*, 120, 584-607.

Colombo, L., Oboe, D., Sbarufatti, C., Cadini, F., Russo, S., & Giglio, M., 2021. Shape sensing and damage identification with iFEM on a composite structure subjected to impact damage and non-trivial boundary conditions. *Mechanical Systems and Signal Processing*, 148, p. 107163.

Davis, M. A., Kersey, A. D., Sirkis, J., & Friebele, E. J., 1996. Shape and vibration mode sensing using a fiber optic Bragg grating array. *Smart Materials and Structures*, 5(6), p. 759.

Esposito, M., & Gherlone, M., 2020. Composite wing box deformed-shape reconstruction based on measured strains: Optimization and comparison of existing approaches. *Aerospace Science and Technology*, 99, p. 105758.

Gherlone, M., Cerracchio, P. & Mattone, M. 2018. Shape sensing methods: Review and experimental comparison on a wing-shaped plate. *Progress in Aerospace Sciences*, 99, 14-26.

Jones, R. T., Bellemore, D. G., Berkoff, T. A., Sirkis, J. S., Davis, M. A., Putnam, M. A., & Kersey, A. D., 1998. Determination of cantilever plate shapes using wavelength division multiplexed fiber Bragg grating sensors and a least-squares strain-fitting algorithm. *Smart Materials and Structures*, 7(2), p. 178.

Kefal, A., & Oterkus, E. 2015. Structural health monitoring of marine structures by using inverse finite element method. *In C. Guedes Soares and R.A. Shenoi (Eds.), Analysis and Design of Marine Structures V*, 341-349.

Kefal, A., Oterkus, E., Tessler, A., & Spangler, J. L. 2016. A quadrilateral inverse-shell element with drilling degrees of freedom for shape sensing and structural health monitoring. *Engineering Science and Technology, an International Journal*, 19, 1299-1313.

Kefal, A., & Oterkus, E. 2016. Displacement and stress monitoring of a Panamax containership using inverse finite element method. *Ocean Engineering*, 119, 16-29.

Kefal, A., & Oterkus, E., 2017. Shape and stress sensing of offshore structures by using inverse finite element method. *In C. Guedes Soares and Y. Garbatov (Eds.), Progress in the Analysis and Design of Marine Structures*, 141-148.

Kefal, A., Tessler, A. & Oterkus, E. 2017. An enhanced inverse finite element method for displacement and stress monitoring of multilayered composite and sandwich structures. *Composite Structures*, 179, 514-540.

Kefal, A., 2019. An efficient curved inverse-shell element for shape sensing and structural health monitoring of cylindrical marine structures. *Ocean Engineering*, 188, p. 106262.

Kefal, A., & Oterkus, E., 2020. Isogeometric iFEM analysis of thin shell structures. *Sensors*, 20(9), p. 2685.

Kefal, A., Tabrizi, I.E., Yildiz, M., & Tessler, A., 2021a. A smoothed iFEM approach for efficient shape-sensing applications: Numerical and experimental validation on composite structures. *Mechanical Systems and Signal Processing*, 152, p. 107486.

Kefal, A., Tabrizi, I.E., Tansan, M., Kisa, E., & Yildiz, M., 2021b. An experimental implementation of inverse finite element method for real-time shape and strain sensing of composite and sandwich structures. *Composite Structures*, 258, p. 113431.

Kim, N. S., & Cho, N. S., 2004. Estimating deflection of a simple beam model using fiber optic Bragg-grating sensors. *Experimental Mechanics*, 44(4), 433-439.

Li, M., Kefal, A., Oterkus, E., & Oterkus, S., 2020. Structural health monitoring of an offshore wind turbine tower using iFEM methodology. *Ocean Engineering*, 204, p. 107291.

Li, M., Kefal, A., Cerik, B.C., & Oterkus, E., 2020. Dent damage identification in stiffened cylindrical structures using inverse finite element method. *Ocean Engineering*, 198, p. 106944.

Liu, M., Zhang, X., Song, H., Zhou, S., Zhou, Z. & Zhou, W., 2018. Inverse finite element method for reconstruction of deformation in the gantry structure of heavy-duty machine tool using FBG sensors. *Sensors*, 18(7), p. 2173.

Miller, E.J., Manalo, R. & Tessler, A., 2016. Full-field reconstruction of structural deformations and loads from measured strain data on a wing test article using the inverse finite element method, NASA TM-2016-219407.

Oboe, D., Colombo, L., Sbarufatti, C., & Giglio, M., 2021. Shape sensing of a complex aeronautical structure with inverse finite element method. *Sensors*, 21(4), p. 1388.

Oboe, D., Colombo, L., Sbarufatti, C., & Giglio, M., 2021. Comparison of strain pre-extrapolation techniques for shape and strain sensing by iFEM of a composite plate subjected to compression buckling. *Composite Structures*, 262, p. 113587.

Papa, U., Russo, S., Lamboglia, A., Del Core, G. & Iannuzzo, G. 2017. Health structure monitoring for the design of an innovative UAS fixed wing through inverse finite element method (iFEM). *Aerospace Science and Technology*, 69, 439-448.

Roy, R., Tessler, A., Surace, C., & Gherlone, M., 2020. Shape sensing of plate structures using the inverse finite element method: Investigation of efficient strain–sensor patterns. *Sensors*, 20(24), p. 7049.

Roy, R., Gherlone, M., Surace, C., & Tessler, A., 2021. Full-field strain reconstruction using uniaxial strain measurements: Application to damage detection. *Applied Sciences*, 11(4), p. 1681.

Tabrizi, I.E., Kefal, A., Zanjani, J.S.M., Akalin, C., & Yildiz, M., 2019. Experimental and numerical investigation on fracture behavior of glass/carbon fiber hybrid composites using acoustic emission method and refined zigzag theory. *Composite Structures*, 223, p. 110971.

Tessler, A., & Spangler, J.L. 2004. Inverse FEM for full-field reconstruction of elastic deformations in shear deformable plates and shells. *In: Proceedings of 2nd European Workshop on Structural Health Monitoring*, Munich, Germany.

Tessler, A., & Spangler, J. L. 2005. A least-squares variational method for full-field reconstruction of elastic deformations in shear-deformable plates and shells. *Computer Methods in Applied Mechanics and Engineering*, 194(2), 327-339.

Tessler, A., Di Sciuva, M., & Gherlone, M., 2010. A consistent refinement of first-order shear deformation theory for laminated composite and sandwich plates using improved zigzag kinematics. *Journal of Mechanics of Materials and Structures*, 5(2), 341-367.